


Progressive Excitability Changes in the Medial Entorhinal Cortex in the 3xTg Mouse Model of Alzheimer's Disease Pathology

Lingxuan Chen,^{1,2} Zoé Christenson Wick,¹ Lauren M. Vetere,¹ Nick Vaughan,¹ Albert Jurkowski,^{1,3} Angelina Galas,^{1,4} Keziah S. Diego,¹ Paul A. Philipsberg,¹ Ivan Soler,¹ Yu Feng,¹ Denise J. Cai,¹ and  Tristan Shuman¹

¹Nash Family Department of Neuroscience, Icahn School of Medicine at Mount Sinai, New York, New York 10029, ²Department of Physiology and Biophysics, University of California, Irvine, Irvine, California 92697, ³Hunter College, City University of New York, New York, New York 10065, and ⁴New York University, New York, New York 10012

Alzheimer's disease (AD) is a chronic neurodegenerative disorder characterized by memory loss and progressive cognitive impairments. In mouse models of AD pathology, studies have found neuronal and synaptic deficits in hippocampus, but less is known about changes in medial entorhinal cortex (MEC), which is the primary spatial input to the hippocampus and an early site of AD pathology. Here, we measured neuronal intrinsic excitability and synaptic activity in MEC layer II (MECII) stellate cells, MECII pyramidal cells, and MEC layer III (MECIII) excitatory neurons at 3 and 10 months of age in the 3xTg mouse model of AD pathology, using male and female mice. At 3 months of age, before the onset of memory impairments, we found early hyperexcitability in intrinsic properties of MECII stellate and pyramidal cells, but this was balanced by a relative reduction in synaptic excitation (E) compared with inhibition (I; E/I ratio), suggesting intact homeostatic mechanisms regulating MECII activity. Conversely, MECIII neurons had reduced intrinsic excitability at this early time point with no change in synaptic E/I ratio. By 10 months of age, after the onset of memory deficits, neuronal excitability of MECII pyramidal cells and MECIII excitatory neurons was largely normalized in 3xTg mice. However, MECII stellate cells remained hyperexcitable, and this was further exacerbated by an increased synaptic E/I ratio. This observed combination of increased intrinsic and synaptic hyperexcitability suggests a breakdown in homeostatic mechanisms specifically in MECII stellate cells at this postsymptomatic time point, which may contribute to the emergence of memory deficits in AD.

Key words: Alzheimer's disease; electrophysiology; excitability; medial entorhinal cortex; stellate cells

Significance Statement

AD causes cognitive deficits, but the specific neural circuits that are damaged to drive changes in memory remain unknown. Using a mouse model of AD pathology that expresses both amyloid and tau transgenes, we found that neurons in the MEC have altered excitability. Before the onset of memory impairments, neurons in layer 2 of MEC had increased intrinsic excitability, but this was balanced by reduced inputs onto the cell. However, after the onset of memory impairments, stellate cells in MEC became further hyperexcitable, with increased excitability exacerbated by increased synaptic inputs. Thus, it appears that MEC stellate cells are uniquely disrupted during the progression of memory deficits and may contribute to cognitive deficits in AD.

Received June 29, 2023; revised Sep. 7, 2023; accepted Sep. 8, 2023.

Author contributions: L.C., Z.C.W., L.M.V., D.J.C., and T.S. designed research; L.C., Z.C.W., L.M.V., N.V., A.J., A.G., K.S.D., P.A.P., I.S., and Y.F. performed research; L.C., Z.C.W., L.M.V., and T.S. analyzed data; L.C., Z.C.W., and T.S. wrote the paper.

This work was supported by National Institutes of Health (NIH)—National Institute on Aging Grants RF1AG072497 (T.S.), and F31AG069496 (L.V.); NIH—National Institute of Neurological Disorders and Stroke Grants R01NS116357 (T.S.), R03NS111493 (T.S.), and F32NS116416 (Z.C.W.); and NIH—National Institute of Mental Health Grants R01MH120162 (D.C.), DP2MH122399 (D.C.), and R56MH132959 (D.C.). We thank all members of the Shuman and Cai labs for comments and feedback throughout this project.

The authors declare no competing financial interests.

Correspondence should be addressed to Tristan Shuman at tristan.shuman@mssm.edu.

<https://doi.org/10.1523/JNEUROSCI.1204-23.2023>

Copyright © 2023 the authors

Introduction

Alzheimer's disease (AD) is an age-related neurodegenerative disorder that is characterized by memory loss and progressive cognitive impairments. Although AD is defined by the presence of amyloid and tau pathology, the causal influence of these pathologies on the development and maintenance of cognitive impairments is poorly understood. In particular, region-specific changes in excitability can precede the buildup of aggregated amyloid (Buckner et al., 2005), suggesting that early changes in cellular and circuit excitability may contribute to cognitive deficits. It is critical, then, to understand the specific

cellular and circuit properties that are altered early in disease progression, even before the onset of cognitive deficits.

The entorhinal cortex is the primary spatial input to the hippocampus and has been implicated as an early site of AD pathology and cell loss in humans (Hyman et al., 1986; Braak and Braak, 1991; Gómez-Isla et al., 1996; Masdeu et al., 2005; Stranahan and Mattson, 2010). In mouse models of AD pathology, studies have found impairments in hippocampus-dependent spatial memory (Billings et al., 2005; Saito et al., 2014) and spatial coding (Cacucci et al., 2008; Mably et al., 2017; Jun et al., 2020), as well as alterations in hippocampal neuronal excitability (Ohno et al., 2004; Brown et al., 2011; Kaczorowski et al., 2011; Davis et al., 2014; Kerrigan et al., 2014; Frazzini et al., 2016) and synaptic transmission (Oddo et al., 2003; Palop and Mucke, 2010; Booth et al., 2016b; Forner et al., 2017; Chen et al., 2018). In addition, spatial coding in the medial entorhinal cortex (MEC) is also disrupted in mouse models of AD pathology (Fu et al., 2017; Ying et al., 2022; Igarashi, 2023) even before the onset of spatial memory impairment (Jun et al., 2020). However, the specific cellular and circuit processes that break down in the MEC to drive altered spatial coding in AD remain unknown.

In MEC layer 2 (MECII), there are 2 major types of excitatory cells, stellate and pyramidal cells, that have distinct electrophysiological properties (Alonso and Klink, 1993; Canto and Witter, 2012; Fuchs et al., 2016). Conversely, in MEC layer 3 (MECIII), the excitatory cells are generally homogenous, with intrinsic properties similar to those of MECII pyramidal cells (Dickson et al., 1997; Gloveli et al., 1997). Importantly, these three excitatory cell types in superficial MEC have distinct major anatomic projections (Suh et al., 2011; Kitamura et al., 2014; Witter et al., 2014; Ohara et al., 2019), and there is some evidence from rodent models of AD pathology that the intrinsic properties of MECII stellate cells may be specifically affected (Stranahan and Mattson, 2010; Marcantoni et al., 2014; Booth et al., 2016a; Heggland et al., 2019). However, the field lacks a thorough examination of each of these populations across the progression of memory impairments.

Here, we followed intrinsic and synaptically generated excitability in MEC across disease progression using the 3xTg mouse model of AD pathology (Oddo et al., 2003; Billings et al., 2005; Javonillo et al., 2022). We performed *in vitro* whole-cell patch-clamp recordings in MECII stellate cells, MECII pyramidal cells, and MECIII excitatory cells in WT and 3xTg mice at early (3 months, before the onset of spatial memory deficits, referred to as presymptomatic) and late (10 months, after spatial memory deficits have emerged, referred to as postsymptomatic) time points and measured both neuronal intrinsic excitability and spontaneous synaptic activity. At the presymptomatic time point, we found changes in excitability in all cell types, but hyperexcitability in MECII stellate and pyramidal cells was balanced by corresponding shifts in the excitation/inhibition (E/I) ratio of synaptic inputs, suggesting strong homeostatic control of overall activity. By the late, postsymptomatic time point, MECII stellate cells showed increases in both intrinsic excitability and synaptic E/I ratio, whereas MECII and MECIII pyramidal cells were mostly normalized. These results suggest that a breakdown in homeostasis drives increased excitability in MECII stellate cells that may contribute to the progression of memory impairments in 3xTg mice.

Materials and Methods

Animals

All experiments were approved in advance by the Institutional Animal Care and Use Committee of the Icahn School of Medicine at Mount Sinai. Both male and female transgenic 3xTg (MMRRC 034830-JAX;

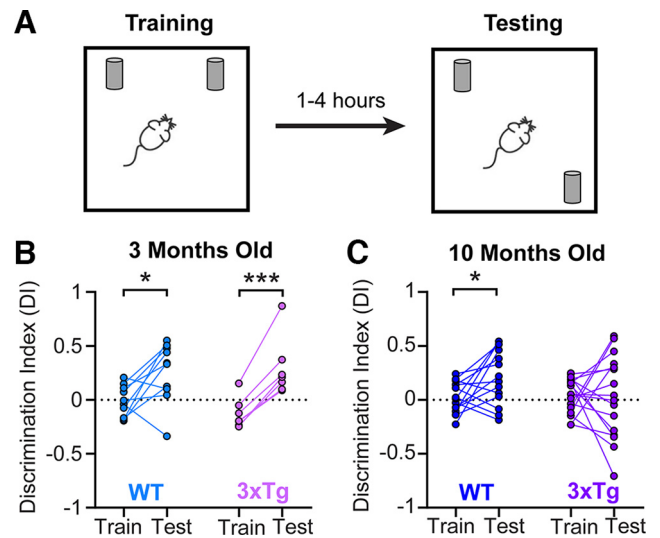


Figure 1. 3xTg mice had intact spatial memory in the novel object location task at 3 months of age but developed a deficit by 10 months of age. **A**, Schematic of the novel object location task. **B**, At 3 months of age, both WT and 3xTg mice showed a preference for the newly located object during the test session, indicated by a significantly increased DI in the testing session compared with the training session (paired *t* test from Train to Test, WT, $p = 0.023$; 3xTg, $p < 0.001$). **C**, At 10 months of age, although WT mice still showed a preference for the moved object in the test session (paired *t* test from Train to Test, WT, $p = 0.037$), 3xTg mice did not (paired *t* test from Train to Test, 3xTg, $p > 0.05$), indicating impaired memory at this late time point. Train, Training; Test, Testing. * $p < 0.05$, *** $p < 0.001$.

Oddo et al., 2003) and wild-type (WT; B6129SF2/J, strain #101045, The Jackson Laboratory; Gstir et al., 2014; Stevens and Brown, 2015) mice were used. Breeders were purchased from the Mutant Mouse Resource and Research Center (MMRRC), and the colony was maintained in approved breeding facilities at Mount Sinai. Mice were given *ad libitum* food and water on a 12 h light/dark cycle (lights on at 0700 h).

Novel object location

Before all experiments, mice were habituated to transportation and handled in the behavior room for 5 d. Mice were then habituated to an empty arena (1 foot \times 1 foot) with spatial cues on the walls for 5 min over 2 consecutive days. The next day, mice were returned to the arena and explored two identical objects (plastic toys $\sim 2 \times 2$ inch) taped near two corners of the arena (training session; Fig. 1A). Mice were then returned to their home cage for 1 or 4 h before testing. During testing, one of the objects was moved to a new location within the arena, and the subject was allowed to freely explore both objects (test session; Fig. 1A). To quantify exploration, we recorded each session with an overhead webcam running Miniscope recording software (Cai et al., 2016; Shuman et al., 2020) and scored interaction bouts using Chronotate, a customized Python application that timestamps user inputs during video playback (Philipsberg et al., 2023; Chronotate available at <https://github.com/ShumanLab/Chronotate>). Interaction was defined as active investigation of the objects, and only the first 15 s of interaction during the test session was used. Mice that had a strong preference for one object [discrimination index (DI) > 0.25 or DI < -0.25] during the training sessions or exclusively interacted with one object during the test sessions were excluded. The DI was calculated as follows:

$$DI =$$

$$\frac{\text{Interaction time with the moved object} - \text{Interaction time with the unmoved object}}{\text{Total interaction time}}$$

Note that we used two slightly different protocols for this experiment. For the 4 h group, mice spent 10 min in the arenas to explore the objects (training session), then 4 h later, spent 10 min in the same arena for the test session. For the 1 h group, the delay between training and

Table 1. Test session DI in the novel object location task with the 1 h and 4 h protocols in WT and 3xTg mice at 3 and 10 months

Group	1 h	4 h	p Value	Test
3 m WT	Values, 0.34, 0.48, −0.34, 0.04, 0.55, 0.12 Mean ± SEM, 0.20 ± 0.13	Values, 0.44, 0.50, 0.10, 0.33 Mean ± SEM, 0.34 ± 0.09	0.4522	Unpaired <i>t</i> test
3 m 3xTg	Values, 0.87, 0.16, 0.37, 0.21, 0.09 Mean ± SEM, 0.34 ± 0.14	Values, 0.23, 0.10 Mean ± SEM, 0.17 ± 0.07	0.4917	Unpaired <i>t</i> test
10 m WT	Values, 0.33, −0.19, 0.54, 0.17, −0.14 Mean ± SEM, 0.25 ± 0.12	Values, 0.06, 0.52, 0.22, −0.08, 0.38, 0.03, 0.12 Mean ± SEM, 0.18 ± 0.08	0.6412	Unpaired <i>t</i> test
10 m 3xTg	Values, 0.04, 0.28, −0.15, 0.30, −0.44, −0.33 Mean ± SEM, 0.00 ± 0.10	Values, 0.15, −0.28, −0.71, 0.59, 0.00, 0.57, 0.45, −0.34 Mean ± SEM, 0.05 ± 0.17	0.7935	Unpaired <i>t</i> test

m, Month; h, Hour.

test was 1 h, and during both training and test an experimenter was counting the interactions of the mice with both objects in real time with a stopwatch. Once mice reached either 30 s of total interaction or 20 min in the box, they were taken out. We observed no difference in the DI of test sessions between these two protocols (Table 1), and the trends from all groups were nearly identical. Thus, we have collapsed across these two delay periods for behavioral analysis. Paired *t* tests were used to compare the DI between training and test sessions within each group (significantly increased DI from training to test indicates learning). One-sample *t* tests were used to determine whether DI during a specific session was different from zero (DI significantly over zero during a test session indicates learning).

In vitro whole-cell patch-clamp recordings

Neuronal intrinsic excitability is an important cellular property that reflects the tendency of a neuron to generate action potentials upon synaptic integration and is critical for learning and memory processes (Daoudal and Debanne, 2003; Zhang and Linden, 2003; Sehgal et al., 2013; Chen et al., 2020). In addition, the activity of a neuron is also tuned by the amount of excitatory and inhibitory synaptic inputs onto the cell. Therefore, it is crucial to probe both neuronal intrinsic excitability and synaptic E/I balance in the same neurons to obtain a thorough assessment of the network state in the healthy and diseased brain.

Mice were anesthetized by isoflurane through inhalation, followed by rapid decapitation. Horizontal acute brain slices were prepared on a vibratome (Leica VT1200 S) at 300 μm thickness in ice-cold cutting solution containing the following (in mM): 135 NMDG, 10 D-glucose, 4 MgCl₂, 0.5 CaCl₂, 1 KCl, 1.2 KH₂PO₄, 20 HEPES, and sucrose to adjust the osmolality to 305–310 mmol/kg, pH 7.35, bubbled with 95% O₂/5% CO₂. Slices were kept in a submerged chamber filled with sucrose-based artificial CSF (sACSF) containing the following (in mM): 55 sucrose, 85 NaCl, 25 D-glucose, 2.5 KCl, 1.25 NaH₂PO₄, 0.5 CaCl₂, 4 MgCl₂, 26 NaHCO₃, 300–305 mmol/kg, bubbled with 95% O₂/5% CO₂. The recovery chamber was kept in a 37°C water bath for 30 min before being held at room temperature.

For whole-cell patch-clamp recordings, acute brain slices were placed in a submerged chamber filled with circulating room temperature ACSF containing the following (in mM): 126 NaCl, 10 D-glucose, 2 MgCl₂, 2 CaCl₂, 2.5 KCl, 1.25 NaH₂PO₄, 1.5 sodium pyruvate, 1 L-glutamine, 295–300 mmol/kg, bubbled with 95% O₂/5% CO₂. No blockers for glutamatergic or GABAergic synaptic transmission were added. A K-methanesulfonate-based intracellular solution containing the following (in mM): 127.5 K-methanesulfonate, 10 HEPES, 5 KCl, 5 Na-phosphocreatine, 2 MgCl₂, 2 Mg-ATP, 0.6 EGTA, and 0.3 Na-GTP, pH 7.25, 285–300 mOsm was used for the current- and voltage-clamp recordings to probe neuronal intrinsic excitability and spontaneous postsynaptic currents, respectively.

Cells were visualized on a Nikon Eclipse FN1 microscope paired with a SOLA Light Engine (Lumencor) to identify cells in MEC layers II or III. A MultiClamp 700B amplifier and an Axon Digidata 1550B digitizer (Molecular Devices) were used for data acquisition. Whole-cell recordings were achieved under voltage clamp at −60 mV. Cells were next switched to current clamp with *I* = 0. Resting membrane potential was measured when cells stabilized. Current-spike curves were determined by injecting a series of current steps (0–500 pA at 50 pA increments, 500 ms) under *I* = 0. The following series of other intrinsic

excitability measurements were taken while cells were held at −70 mV: (1) rheobase, calculated as the current needed to generate the first action potential by injecting a series of 500 ms current steps at 10 pA increments; (2) input resistance, calculated as $R_{in} = V/I$, at *I* = −50 pA; (3) spike amplitude, amplitude of the first stimulated spike; (4) spike half-width: width of the first stimulated spike at its half maximal value; (5) medium afterhyperpolarization (mAHP), calculated as the lowest point of the postburst hyperpolarization relative to baseline, averaged over five 500 ms, 500 pA current steps; (6) slow AHP (sAHP), calculated as the remaining hyperpolarization 1.5 s after the end of stimulation, averaged over five 500 ms, 500 pA current steps; and (7) sag ratio, the amount of sag potential during a hyperpolarizing current step (*I* = −100 pA), calculated as (lowest point of hyperpolarization − steady-state voltage at the end of current step) / (lowest point of hyperpolarization − prestep baseline). After these measurements, cells were switched back to voltage clamp at *V* = −60 mV to record 90 s of spontaneous EPSCs, then slowly depolarized to *V* = 0 mV to record 90 s of spontaneous IPSCs. For each cell, the frequency of spontaneous postsynaptic currents was calculated as one divided by the average of all interevent intervals, and the amplitude was averaged across all detected events. Ratios of excitatory to inhibitory frequency or amplitude (E/I ratios) were calculated for each cell before being compared across genotypes. Clampfit 10.7 software (Molecular Devices) was used for processing electrophysiology data. Action potential measurements were done using the Threshold Search mode under Event Detection. Recordings acquired under voltage clamp were first filtered with a Gaussian low-pass filter. Then EPSCs and IPSCs were detected using the Template Search mode, using cell-based templates. Detected events also went through a visual inspection to exclude any outliers or noise.

Experimental design and statistical analyses

To exclude the effect of prior experience on the excitability of MEC neurons, we used separate groups of mice for behavior and electrophysiological experiments. Both male and female mice were used. The number of mice of each sex used for behavior and patch-clamp recordings and the total number of cells recorded are listed in Table 2. For each experiment, the number of cells (*n*) and number of animals (*N*) are given in the corresponding figure legends. To determine the progression of memory deficits in the 3xTg model for the novel object location task (Fig. 1), mice at 2.3–4.1 months and 9.2–11.5 months of age were used for groups 3 months and 10 months, respectively. To examine intrinsic and synaptic excitability at the early and late time points, mice at 3.3–4.0 months and 9.0–11.6 months of age were used for groups 3 m and 10 m, respectively, for whole-cell patch-clamp recordings.

Clustering MECII neurons into stellate and pyramidal cells. During whole-cell patch-clamp recordings in layer II of MEC, experimenters provided a preliminary identification of whether a cell was stellate or pyramidal by its morphology under the microscope and the action potential firing pattern. To provide an unbiased approach, we clustered MECII neurons into two subtypes based on electrophysiological parameters. The previous literature has indicated significantly larger hyperpolarizing sag currents (Alonso and Klink, 1993; Canto and Witter, 2012; Fuchs et al., 2016; Fernandez et al., 2022) and AHPs (Alonso and Klink, 1993) in stellate cells compared with pyramidal cells in MECII. Therefore, we used *k*-means clustering to divide cells into two sets based on the sag ratio and mAHP (see above, *In vitro*

Table 2. Number of animals (N) of each sex and number of recorded cells (n)

	3 m WT	3 m 3xTg	10 m WT	10 m 3xTg
Novel object location (1 h delay)				
N of males	3	3	4	6
N of females	3	2	3	2
Novel object location (4 h delay)				
N of males	2	0	3	3
N of females	2	2	4	5
MECII recordings				
N of males	1	3	2	1
n of males	1	15	2	2
n (stellate) of males	0	8	0	2
n (pyramidal) of males	1	7	2	0
N of females	9	5	7	6
n of females	29	19	30	24
n (stellate) of females	7	13	11	14
n (pyramidal) of females	22	6	19	10
MECIII recordings				
N of males	0	0	3	0
n of males	0	0	9	0
N of females	4	3	1	4
n of females	12	13	1	10

m, Month.

whole-cell patch-clamp recordings), which gave clear separation between clusters (Fig. 2). To accommodate potential age-related changes, we performed the *k*-means clustering on 3 month (Fig. 2A–C) and 10 month (Fig. 2D–F) data separately. Note that WT and 3xTg cells at each time point were clustered together, but for the purpose of visualization they were separately plotted. We also visually inspected the automated clustering to ensure proper performance of the algorithm. Based on visual inspection of the clusters plus the preliminary identification of cell type during patching, we manually changed the cluster of one cell in the 3 month 3xTg group and one cell in the 10 month WT group and excluded two cells in the 3-month WT group that lay on the borderline between clusters. These changes were made while blind to all other excitability measurements. In addition, there were six cells in the 3 month 3xTg group and five cells in the 10-month 3xTg group that did not have mAHP measurements. These 11 cells are not shown in Figure 2. They were only manually clustered as stellate cells if (1) sag ratio was >0.3, and (2) during recording they were visually determined to be stellate cells. Otherwise, they were clustered as pyramidal cells.

Data analysis and statistics of patch-clamp recordings. Current-evoked action potentials under current clamp and postsynaptic currents under voltage clamp were detected using Clampfit 10.7 software (Molecular Devices) plus a visual inspection (see above, In vitro whole-cell patch-clamp recordings). Statistical analyses were performed with Prism 9 software (GraphPad). For all analyses, outliers in each data group were first identified with the ROUT (robust regression and outlier removal) method, $Q = 1\%$, and excluded from the dataset. All cells with outlier values in the EPSC or IPSC calculations were also excluded from the E/I ratio calculations. Then, normality was determined using the Shapiro–Wilk test. An unpaired *t* test was used for normally distributed data, and a Mann–Whitney test was used for data that was not normally distributed. For all graphs, data are represented as mean \pm SEM. For comparisons between the current-spike curves, cells that did not receive all the current steps from 0 to 500 pA (for MECII neurons) or from 0 to 300 pA (for MECIII neurons) were excluded, and two-way repeated-measures ANOVA (RM ANOVA) was used to test for statistical differences between genotypes.

Results

Impaired spatial memory in 10-month-old but not 3-month-old 3xTg mice

To examine the progression of spatial memory deficits in the 3xTg mouse model of AD pathology, we used a novel object

location task (Fig. 1A) that is dependent on both hippocampus (Murai et al., 2007; Wimmer et al., 2012) and MEC (Tennant et al., 2018). During initial training, WT and 3xTg mice investigated two identical objects, showing no preference for one over another, indicated by a DI that was not significantly different from zero, at either 3 months (Fig. 1B; Train, one-sample *t* test, $p > 0.05$ for both WT and 3xTg mice) or 10 months of age (Fig. 1C; Train, one-sample *t* test, $p > 0.05$ for both WT and 3xTg mice). During testing, the animals were returned to the arena 1 or 4 h later with one object moved to a new location (see above, Materials and Methods; Tables 1 and 2). In 3-month-old mice, both WT and 3xTg mice showed a preference for the newly located object (Fig. 1B; Test, one-sample *t* test, WT, $p = 0.016$, $N = 10$; 3xTg, $p = 0.030$, $N = 7$; paired *t* test from training to testing, WT, $p = 0.023$, 3xTg, $p < 0.001$), indicating an intact spatial memory of the unmoved object. In contrast, in 10-month-old mice, only the WT mice showed significant learning during the test (Fig. 1C; Test, one-sample *t* test, WT, $p = 0.009$, $N = 14$; paired *t* test from training to testing, WT, $p = 0.037$). Ten-month-old 3xTg mice did not show a preference for the moved object (Fig. 1C; Test, one-sample *t* test, 3xTg, $p > 0.05$, $N = 16$; paired *t* test from training to testing, 3xTg, $p > 0.05$), suggesting impaired spatial memory at this late time point.

Overall, these results show that spatial memory deficits are age dependent and emerge between 3 and 10 months of age in the 3xTg mice, consistent with previous reports (Billings et al., 2005; Davis et al., 2013; Belfiore et al., 2019; Creighton et al., 2019). Therefore, we used 3- and 10-month-old mice for our pre-symptomatic and postsymptomatic time points for all additional experiments.

Classification of MECII cells into stellate and pyramidal cells in 3- and 10-month-old WT and 3xTg mice based on electrophysiological properties

The cell types in MECII and MECIII have been well characterized based on morphologic, immunohistochemical, and electrophysiological evidence over the past few decades (Alonso and Klink, 1993; Klink and Alonso, 1997; Varga et al., 2010; Canto and Witter, 2012; Kitamura et al., 2014; Ray et al., 2014). In MECII, stellate cells have distinct intrinsic electrophysiological properties not present in MECII pyramidal cells, such as significant hyperpolarizing sag potentials, burst firing, and depolarizing afterpotentials (Alonso and Klink, 1993; Canto and Witter, 2012; Fuchs et al., 2016; Fernandez et al., 2022). This allowed us to identify MECII stellate versus pyramidal cells based on these intrinsic properties. We found that the sag ratio (at -100 pA current step) and mAHP amplitudes best isolated the clusters of MECII neurons in our recordings (Fig. 2; see above, Materials and Methods). In accordance with the literature, stellate cells were identified as the cluster with high sag potential and large mAHP (Fig. 2A,B,D,E; above dashed lines), and pyramidal cells were identified as the cluster with low sag ratio and small mAHP (below dashed lines). To further validate our cell-type classification, we have plotted MECIII cells in the same space (Fig. 2C,F). Because layer III neurons have been shown to have properties similar to those of MECII pyramidal cells (Dickson et al., 1997; Gloveli et al., 1997), they should all fall into the pyramidal cluster. Indeed, all 3 m and 10 m MECIII cells fell below the dashed line (Fig. 2C,F). In addition to validating our MECII clustering, this also supported the identification of MECIII neurons as pyramidal cells. Together, this clustering strategy allowed us to identify MECII stellate cells, MECII pyramidal cells, and MECIII

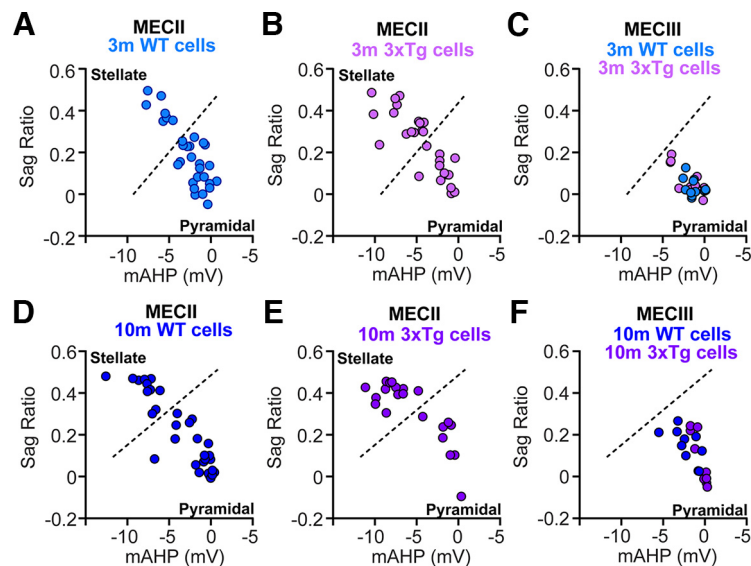


Figure 2. MECII neurons were clustered into stellate- and pyramidal-like cells based on their electrophysiological properties, whereas MECIII neurons had properties similar to those of pyramidal cells. **A, B, D, E,** Using *k*-means clustering, MECII neurons recorded at 3 months (**A**, $n = 30$ cells from 10 WT mice; **B**, $n = 28$ cells from 7 3xTg mice) and 10 months (**D**, $n = 32$ cells from 9 WT mice; **E**, $n = 21$ from 5 3xTg mice) of age were separated into two clusters based on the sag ratio and mAHP of each neuron. Neurons with large sag ratios and mAHPs were clustered as stellate-like cells (above the dashed line), and those with small sag ratios and mAHPs were clustered as pyramidal cells (below the dashed line). WT and 3xTg cells were clustered, but for the purpose of visualization, they were separately plotted. **C, F,** Three-month (**C**, $n = 12$ cells from 4 WT mice; $n = 13$ from 3 3xTg mice) and 10-month (**F**, $n = 9$ from 4 WT mice; $n = 10$ from 4 3xTg mice) MECIII cells recorded from WT and 3xTg mice all fell into the pyramidal cell cluster when using the same criteria as layer II data (**A, B, D, E**).

excitatory neurons based on their well-characterized intrinsic properties.

Early changes in neuronal excitability are balanced by corresponding changes in synaptic inputs in MECII and MECIII cells of 3xTg mice at the presymptomatic time point

To test for changes in neuronal excitability at the early presymptomatic time point, we performed whole-cell patch-clamp recordings in the MEC of 3xTg and WT mice at 3 months of age (Table 2, number of mice and cells recorded). In MECII stellate cells of 3xTg mice (Fig. 3), we found evidence of enhanced intrinsic excitability at this early time point. Although the resting membrane potential of 3xTg MECII stellate cells was comparable to that of WT cells (Fig. 3A; unpaired *t* test, $p > 0.05$), the rheobase, defined as the minimum current needed to elicit an action potential, of 3xTg cells was significantly reduced (Fig. 3B; unpaired *t* test, $p = 0.009$). Further, the number of evoked action potentials in response to current injections of increasing size was significantly increased in 3xTg cells (Fig. 3C; two-way RM ANOVA, main effect of genotype, $p = 0.001$). These results indicate that there is intrinsic hyperexcitability in MECII stellate cells in 3xTg mice at 3 months, before the onset of cognitive deficits. However, when we looked at spontaneous EPSCs and IPSCs in the same stellate cells, we found that the ratio of excitatory to inhibitory inputs (E/I ratios) was altered. Specifically, we found that both the ratios of E/I frequency and E/I amplitude were significantly skewed toward inhibition, suggesting relatively more robust inhibitory inputs to MECII stellate cells in 3xTg mice (Fig. 3G; E/I frequency, unpaired *t* test, $p = 0.007$; Fig. 3K; E/I amplitude, Mann–Whitney, $p = 0.031$). In particular, the reduction in the ratio of E/I amplitude was primarily caused by increased IPSC amplitude in 3xTg mice (Fig. 3I; IPSC amplitude, Mann–Whitney, $p = 0.025$). Together, these opposing changes to intrinsic and synaptic excitability, which are likely a combination of pathologic and compensatory homeostatic changes, may result in little to no net change in neuronal activity in 3-month-old 3xTg mice.

We next examined MECII pyramidal cells at the same early time point and found a similar increase in neuronal excitability and decreased ratio of E/I inputs onto these cells in 3xTg mice (Fig. 4). At this early time point, MECII pyramidal cells in 3xTg mice displayed no change in resting membrane potential (Fig. 4A; unpaired *t* test, $p > 0.05$), but did show decreased rheobase (Fig. 4B; unpaired *t* test, $p = 0.001$) and an increased number of current-evoked action potentials (Fig. 4C; two-way RM ANOVA, main effect of genotype, $p = 0.002$) compared with WT mice. Synaptic E/I ratio was also reduced in layer II pyramidal cells of 3xTg mice (Fig. 4G; E/I frequency, Mann–Whitney, $p = 0.020$; Fig. 4K; E/I amplitude, unpaired *t* test, $p = 0.003$), similarly skewing toward relatively more inhibitory than excitatory inputs. In contrast to the stellate cells, however, the decreased synaptic E/I ratio in MECII pyramidal cells was mainly driven by reduced excitation (Fig. 4D; EPSC frequency, Mann–Whitney, $p = 0.005$; Fig. 4H, EPSC amplitude, unpaired *t* test, $p = 0.063$). Thus, at an early presymptomatic time point, both MECII stellate cells and MECII pyramidal cells have increased intrinsic excitability that is concurrent with a relative enhancement of inhibition in the E/I ratio of synaptic inputs. However, each cell type appears to have distinct mechanisms driving these changes in synaptic currents, with MECII stellate cells receiving enhanced inhibitory inputs and MECII pyramidal cells receiving fewer excitatory inputs.

In contrast to layer II cells, MECIII neurons of 3-month-old 3xTg mice showed reduced intrinsic excitability at this early presymptomatic time point (Fig. 5). This was seen in the reduced number of current-evoked action potentials in 3xTg MECIII pyramidal cells compared with WT (Fig. 5C; two-way RM ANOVA, main effect of genotype, $p = 0.009$), despite no change in resting membrane potential or rheobase (Fig. 5A,B). Meanwhile, 3xTg MECIII pyramidal cells were receiving more frequent synaptic inhibition (Fig. 5E; IPSC Frequency, unpaired *t* test, $p = 0.018$) and stronger excitatory inputs (Fig. 5H; EPSC amplitude, unpaired *t* test, $p = 0.003$), resulting in an overall E/I ratio that remained

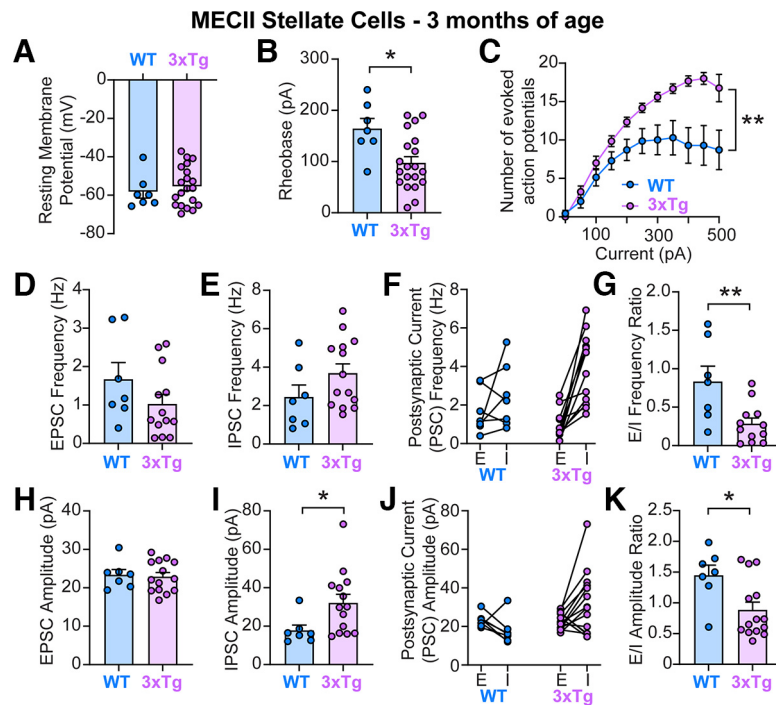


Figure 3. At 3 months of age, MECII stellate cells in 3xTg mice had increased neuronal intrinsic excitability, which was balanced by increased synaptic inhibition and decreased synaptic E/I ratio. **A–C**, Neuronal intrinsic excitability of MECII stellate cells was increased in 3xTg mice compared with controls, indicated by a reduced rheobase (**B**, unpaired *t* test, $p = 0.009$) and an increased number of current-evoked action potentials (**C**, $n = 7$ cells from WT mice; $n = 12$ cells from 3xTg mice; two-way RM ANOVA, main effect of genotype, $p = 0.001$). **D–K**, Meanwhile, there was increased synaptic inhibition onto these stellate cells, demonstrated by a larger IPSC amplitude (**I**, Mann–Whitney test, $p = 0.025$) and an overall decrease in synaptic E/I ratio both in frequency (**G**, unpaired *t* test, $p = 0.007$) and amplitude (**K**, Mann–Whitney test, $p = 0.031$). Within each cell, excitatory (E) and inhibitory (I) currents were measured (**F**, **J**), and the E/I ratio was calculated for each individual cell and then compared between genotypes (**G**, **K**). All other tests showed no differences between groups ($p > 0.05$). * $p < 0.05$. ** $p < 0.01$.

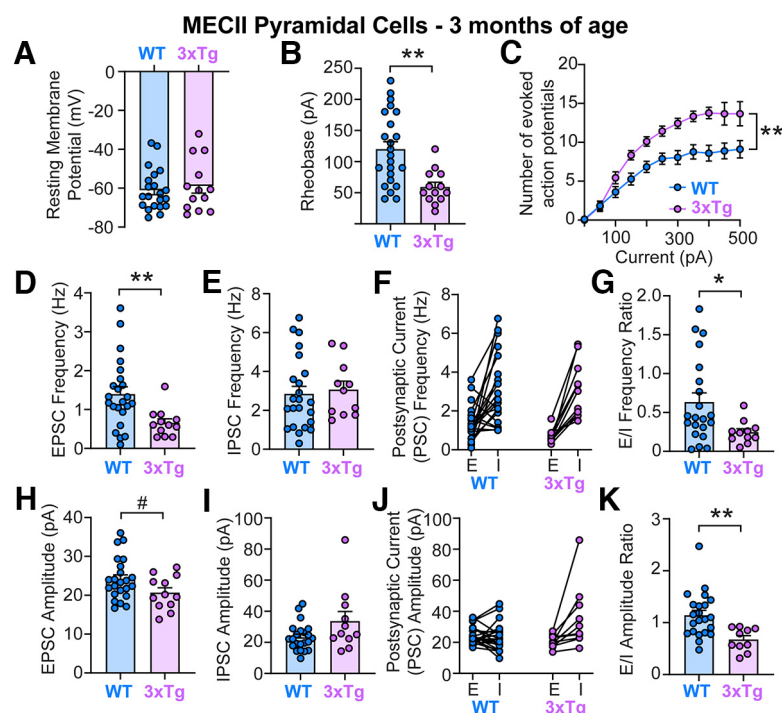


Figure 4. At 3 months of age, MECII pyramidal cells in 3xTg mice had increased neuronal intrinsic excitability, which was balanced by decreased synaptic excitation and decreased synaptic E/I ratio. **A–C**, Similar to stellate cells, neuronal intrinsic excitability of MECII pyramidal cells was increased in 3xTg mice compared with controls, indicated by a reduced rheobase (**B**, unpaired *t* test, $p = 0.001$) and an increased number of current-evoked action potentials (**C**, $n = 18$ cells from WT mice; $n = 9$ cells from 3xTg mice; two-way RM ANOVA, main effect of genotype, $p = 0.002$). **D–K**, Meanwhile, there was decreased synaptic excitation onto these pyramidal cells, demonstrated by a reduced EPSC frequency (**D**, Mann–Whitney test, $p = 0.005$) and an overall decrease in synaptic E/I ratio both in frequency (**G**, Mann–Whitney test, $p = 0.020$) and amplitude (**K**, unpaired *t* test, $p = 0.003$). There was also a trend for a decrease in EPSC amplitude (**H**, unpaired *t* test, $p = 0.063$). Within each cell, excitatory (E) and inhibitory (I) currents were measured (**F**, **J**), and the E/I ratio was calculated for each individual cell and then compared between genotypes (**G**, **K**). All other tests showed no differences between groups ($p > 0.05$). * $p < 0.05$. ** $p < 0.01$. # marginally significant.

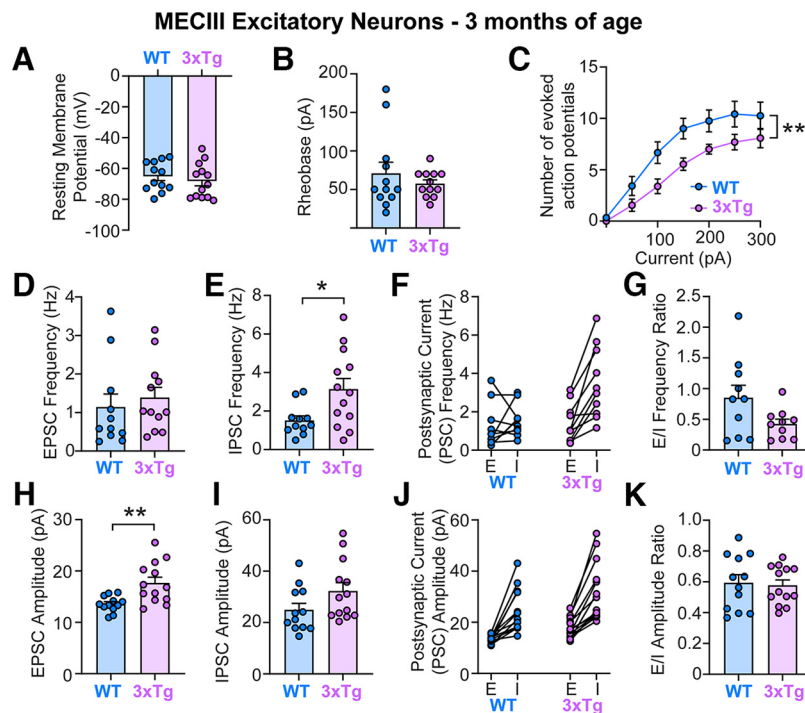


Figure 5. At 3 months of age, MECIII cells in 3xTg mice had decreased neuronal intrinsic excitability with no change in synaptic E/I ratio. **A–C**, In contrast to layer II neurons, MECIII neurons showed decreased neuronal intrinsic excitability, indicated by a reduced number of current-evoked action potentials (**C**, $n = 12$ cells from WT mice; $n = 13$ cells from 3xTg mice; two-way RM ANOVA, main effect of genotype, $p = 0.009$). **D–K**, In the same cells, there was an increase in the amplitude of EPSCs (**H**, unpaired t test, $p = 0.003$) and an increase in the frequency of IPSCs (**E**, unpaired t test, $p = 0.018$), but there were no changes in the synaptic E/I ratio in either frequency (**G**) or amplitude (**K**) of synaptic currents. Within each cell, excitatory (E) and inhibitory (I) currents were measured (**F**, **J**), and the E/I ratio was calculated for each individual cell and then compared between genotypes (**G**, **K**). All other tests showed no differences between groups ($p > 0.05$). * $p < 0.05$. ** $p < 0.01$.

Table 3. Neuronal intrinsic excitability measurements—early time point (3 months)

	3 m WT	3 m 3xTg	p Value	Test
MECII Stellate cells				
Input resistance ($M\Omega$)	89.98 \pm 8.48	112.6 \pm 10.98	0.1871	Unpaired t test
Spike amplitude (mV)	85.55 \pm 2.25	84.26 \pm 1.94	0.7227	Unpaired t test
Spike half-width (ms)	1.88 \pm 0.16	1.48 \pm 0.07	*0.0101	Mann–Whitney
mAHP (mV)	−6.04 \pm 0.45	−6.59 \pm 0.56	0.5392	Unpaired t test
sAHP (mV)	−0.45 \pm 0.09	−0.26 \pm 0.08	0.1549	Unpaired t test
Sag ratio	0.41 \pm 0.02	0.36 \pm 0.02	0.1395	Unpaired t test
MECII pyramidal cells				
Input resistance ($M\Omega$)	139.9 \pm 12.96	221.1 \pm 18.50	***0.0005	Mann–Whitney
Spike amplitude (mV)	82.92 \pm 2.01	86.24 \pm 3.28	0.2668	Mann–Whitney
Spike half-width (ms)	1.83 \pm 0.05	1.68 \pm 0.12	0.1742	Unpaired t test
mAHP (mV)	−1.64 \pm 0.26	−1.85 \pm 0.35	0.6325	Unpaired t test
sAHP (mV)	−0.35 \pm 0.07	−0.72 \pm 0.15	*0.0181	Unpaired t test
Sag ratio	0.13 \pm 0.02	0.11 \pm 0.02	0.4911	Unpaired t test
MECIII cells				
Input resistance ($M\Omega$)	257.6 \pm 27.16	229.0 \pm 20.52	0.4044	Unpaired t test
Spike amplitude (mV)	84.78 \pm 1.90	86.63 \pm 1.78	0.4852	Unpaired t test
Spike half-width (ms)	1.64 \pm 0.06	1.92 \pm 0.11	#0.0523	Mann–Whitney
mAHP (mV)	−1.26 \pm 0.27	−1.84 \pm 0.40	0.2455	Unpaired t test
sAHP (mV)	−1.03 \pm 0.24	−0.58 \pm 0.22	0.1801	Unpaired t test
Sag ratio	0.03 \pm 0.01	0.06 \pm 0.02	0.1683	Mann–Whitney

m, Month. * $p < 0.05$. ** $p < 0.01$. *** $p < 0.001$. # marginally significant.

comparable to age-matched WT mice (Fig. 5G; E/I Frequency and Fig. 5K; E/I amplitude, $p > 0.05$).

In addition to quantifying resting membrane potential, rheobase, and the current-spike relationship, we also quantified several other intrinsic excitability measures in MECII stellate cells and MECII and MECIII pyramidal cells from 3-month-old WT and

3xTg mice (Table 3). In general, these additional measurements supported the main findings in Figures 3–5. MECII stellate and pyramidal cells displayed early neuronal hyperexcitability (decreased spike half-width in stellate cells and increased input resistance in pyramidal cells; Table 3), and MECIII cells showed early hypoexcitability (a trend toward increased spike half-width, $p = 0.052$; Table 3) in 3xTg mice. We also found that MECII pyramidal cells had an enlarged postburst sAHP, which would likely reduce overall excitability (Disterhoft and Oh, 2006; Oh et al., 2010) and may serve as compensation for the early hyperexcitability seen in other measures (i.e., Fig. 4B,C; reduced rheobase and increased stimulated action potential firing; Table 3, increased input resistance).

Together, these data demonstrate that at an early time point in the 3xTg mice, before the onset of MEC-hippocampus-dependent memory impairment (Fig. 1B), there were already intrinsic and synaptic changes in all the three major types of MECII and MECIII excitatory neurons. Remarkably, excitability changes at the neuronal and synaptic levels primarily moved in opposite directions, suggesting robust homeostatic regulation in this circuit that may allow it to maintain proper function. Notably, although MECII stellate and pyramidal cells underwent similar changes in the E/I ratio of synaptic currents, their mechanisms were distinct. Hyperexcitable stellate cells received relatively more inhibition, whereas hyperexcitable pyramidal cells received less excitation, both resulting in a reduced synaptic E/I ratio. This indicates cell-type-specific reorganization of synaptic inputs are occurring already at this early time point. These changes between intrinsic and synaptic excitability may result in the maintenance of normal levels of overall excitability in MECII and thus relatively

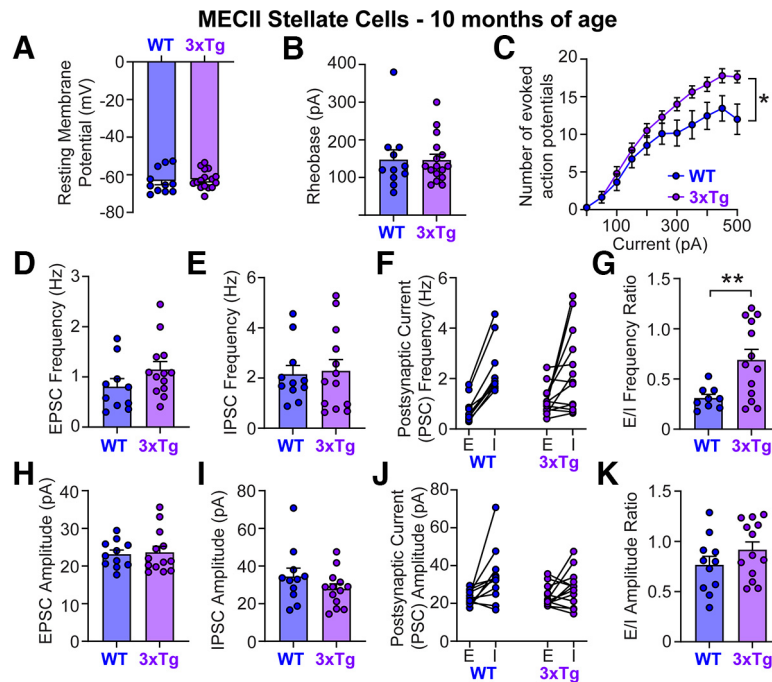


Figure 6. At 10 months of age, MECII stellate cells showed increases in both neuronal intrinsic excitability and synaptic E/I ratio. **A–C**, There was an increased number of current-evoked action potentials in stellate cells of 3xTg mice (**C**, $n = 11$ cells from WT mice; $n = 14$ cells from 3xTg mice; two-way RM ANOVA, main effect of genotype, $p = 0.048$). **D–K**, Meanwhile, the E/I ratio of the frequency of synaptic currents was increased in 3xTg stellate cells (**G**, unpaired t test, $p = 0.009$). Within each cell, excitatory (E) and inhibitory (I) currents were measured (**F**, **J**), and the E/I ratio was calculated for each individual cell and then compared between genotypes (**G**, **K**). All other tests showed no differences between groups ($p > 0.05$). * $p < 0.05$. ** $p < 0.01$.

normal inputs to the dentate gyrus early in AD, before the onset of spatial memory deficits. Regardless, these changes in neuronal and synaptic excitability were not sufficient to drive spatial memory deficits at this early time point (Fig. 1B).

Development of combined intrinsic and synaptic hyperexcitability specifically in MECII stellate cells of 3xTg mice at the late, postsymptomatic time point

To test how intrinsic and synaptic excitability in MEC neurons were altered in 3xTg mice after the onset of spatial memory deficits, we again performed whole-cell patch-clamp recordings in MECII stellate cells of 3xTg and WT mice at 10 months of age (Fig. 6, Table 2, number of mice and cells recorded). In 3xTg mice, MECII stellate cells continued to have increased intrinsic excitability at this late time point, with an elevated number of current-evoked action potentials (Fig. 6C; two-way RM ANOVA, main effect of genotype, $p = 0.047$). However, in contrast to the early time point that showed reduced synaptic E/I ratios (Fig. 3G,K), at 10 months of age, MECII stellate cells in 3xTg mice had an increased synaptic E/I frequency compared with WT mice (Fig. 6G; E/I frequency, unpaired t test, $p = 0.009$). Together, the heightened intrinsic excitability and synaptic E/I ratio may work synergistically to cause overall hyperexcitability in MECII stellate cells in 10-month-old 3xTg mice. Surprisingly, intrinsic and synaptic excitability were largely normalized in MECII pyramidal cells at this time point (Fig. 7). In MECII pyramidal neurons, we found no differences in resting membrane potential, rheobase, current-evoked action potentials, the frequency or amplitude of synaptic currents, or in the E/I balance of synaptic currents (Fig. 7; $p > 0.05$ for all tests). In MECIII pyramidal cells, we found a more hyperpolarized resting membrane potential in 3xTg mice (Fig. 8A; unpaired t test, $p = 0.035$), but

there was no change in rheobase or current-evoked firing (Fig. 8B,C). Meanwhile, synaptic excitation increased in these cells (Fig. 8D; EPSC frequency, Mann–Whitney, $p = 0.004$) but was mostly matched by a trend toward increased inhibition (Fig. 8E; IPSC frequency, Mann–Whitney, $p = 0.073$), leading to similar E/I ratios between 3xTg and WT mice (Fig. 8G,K). Therefore, the balance between intrinsic and synaptic excitability was generally maintained in MECIII pyramidal cells.

When we looked into other intrinsic excitability properties at this late time point, significant reductions in spike half-width emerged in MECII stellate and pyramidal cells, pointing to increased neuronal excitability in 3xTg mice (Table 4). In MECIII pyramidal cells, although there was a hyperpolarized resting membrane potential (Fig. 8A), there was also a significantly reduced mAHP and a trend toward a reduced sAHP (Table 4) pointing to increased excitability (Disterhoft and Oh, 2006; Oh et al., 2010). This may reflect homeostatic compensation between the hyperpolarized membrane potential and the AHP amplitudes that may allow MECIII pyramidal cells to maintain relatively normal firing rates in 3xTg mice at 10 months of age.

Together, these results highlight a cell-type-specific shift toward overall hyperexcitability in MECII stellate cells at the late postsymptomatic time point in the 3xTg mouse model of AD pathology. Notably, the increased synaptic inhibition that was observed at 3 months of age was not present at 10 months of age, and instead the E/I ratio switched from a shift toward inhibition to a shift toward excitation during the emergence of spatial memory impairments in 3xTg mice. These intrinsic and synaptic alterations drive MECII stellate cell hyperexcitability at this late time point, which may drive changes in the downstream hippocampal activity and the emergence of memory impairments. Importantly, this overall hyperexcitability, with both intrinsic and synaptic changes strongly driving increased

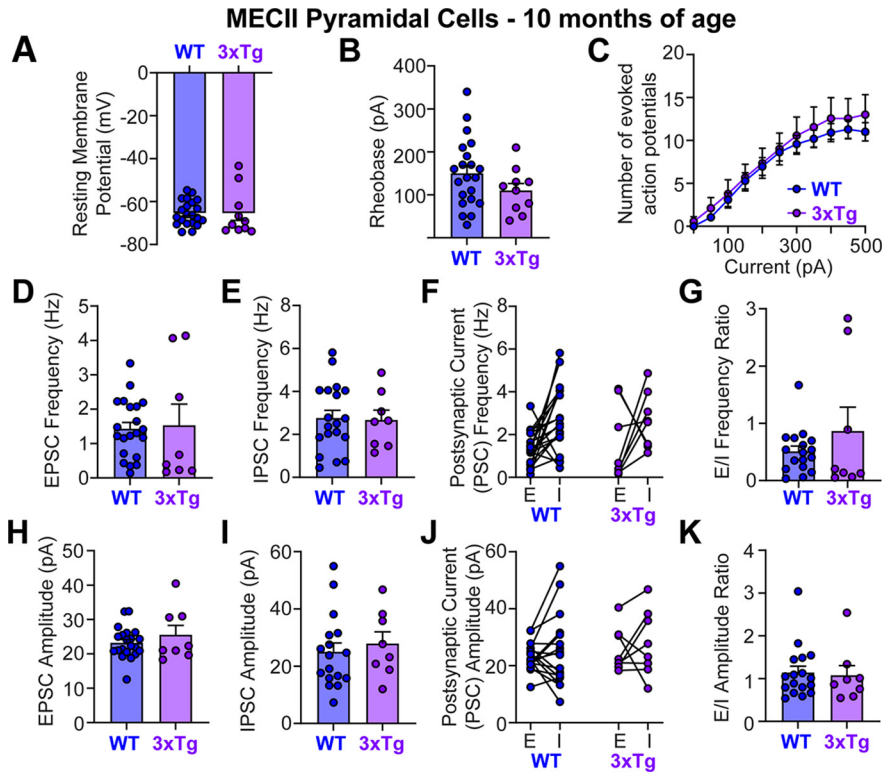


Figure 7. At 10 months of age, intrinsic and synaptic excitability was mostly normalized in MECII pyramidal cells in 3xTg mice. For MECII pyramidal cells, both neuronal intrinsic excitability (A–C) and synaptic E and I (D–K) in 3xTg mice were comparable to those in WT mice (all tests, $p > 0.05$). Within each cell, excitatory (E) and inhibitory (I) currents were measured (F, J), and the E/I ratio was calculated for each individual cell and then compared between genotypes (G, K).

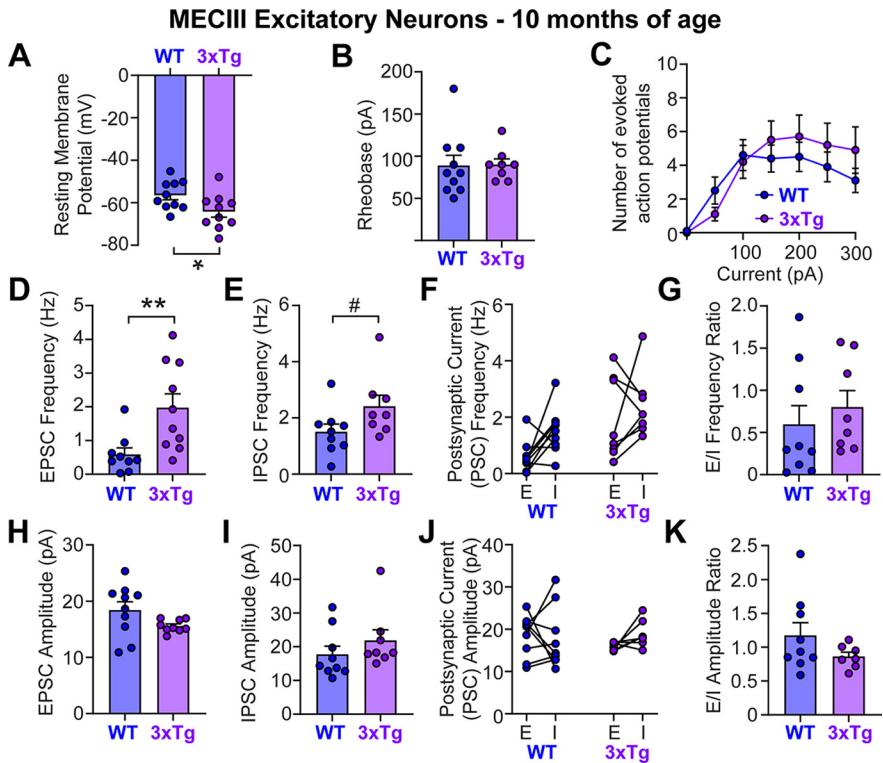


Figure 8. At 10 months of age, MECIII cells in 3xTg were hyperpolarized, whereas no change was found in synaptic E/I ratio. A–C, For MECIII neurons, cells in 3xTg mice had a hyperpolarized resting membrane potential (RMP; A, unpaired t test, $p = 0.035$), whereas the rheobase and number of current-evoked action potentials remained comparable to that in WT mice (B, C). D–K, In 3xTg mice, the frequency of EPSCs was increased (D, Mann–Whitney test, $p = 0.004$), and there was a trend for an increase in IPSC frequency (E, unpaired t test, WT versus 3xTg, $p = 0.073$). However, the synaptic E/I ratio did not differ between 3xTg and WT cells in either the frequency (G) or amplitude (K) of synaptic currents. Within each cell, excitatory (E) and inhibitory (I) currents were measured (F, J), and the E/I ratio was calculated for each individual cell and then compared between genotypes (G, K). All other tests showed no differences between groups ($p > 0.05$). * $p < 0.05$. ** $p < 0.01$. # marginally significant.

Table 4. Neuronal intrinsic excitability measurements—late time point (10 months)

	10 m WT	10 m 3xTg	<i>p</i> Value	Test
MECII Stellate cells				
Input resistance (MΩ)	78.59 ± 8.57	79.13 ± 5.95	0.9581	Unpaired <i>t</i> test
Spike amplitude (mV)	85.65 ± 1.09	81.28 ± 1.75	*0.0444	Unpaired <i>t</i> test
Spike half-width (ms)	1.38 ± 0.03	1.28 ± 0.04	*0.0069	Mann–Whitney
mAHP (mV)	−7.99 ± 0.53	−8.14 ± 0.46	0.5038	Mann–Whitney
sAHP (mV)	−0.34 ± 0.05	−0.30 ± 0.04	0.5404	Unpaired <i>t</i> test
Sag ratio	0.42 ± 0.02	0.42 ± 0.01	0.4510	Mann–Whitney
MECII pyramidal cells				
Input resistance (MΩ)	158.4 ± 21.74	155.9 ± 16.56	0.3927	Mann–Whitney
Spike amplitude (mV)	75.82 ± 2.87	81.29 ± 2.37	0.2866	Mann–Whitney
Spike half-width (ms)	1.84 ± 0.10	1.38 ± 0.05	***0.0005	Mann–Whitney
mAHP (mV)	−1.49 ± 0.41	−1.38 ± 0.48	0.6224	Mann–Whitney
sAHP (mV)	−0.45 ± 0.12	−0.28 ± 0.09	0.9332	Mann–Whitney
Sag ratio	0.11 ± 0.02	0.16 ± 0.04	0.1244	Mann–Whitney
MECIII cells				
Input resistance (MΩ)	267.3 ± 15.71	225.5 ± 30.65	0.2408	Unpaired <i>t</i> test
Spike amplitude (mV)	64.08 ± 1.86	67.35 ± 2.72	0.3350	Unpaired <i>t</i> test
Spike half-width (ms)	2.09 ± 0.17	1.92 ± 0.11	0.4054	Unpaired <i>t</i> test
mAHP (mV)	−2.41 ± 0.53	−0.56 ± 0.25	**0.0048	Unpaired <i>t</i> test
sAHP (mV)	−0.38 ± 0.09	−0.12 ± 0.09	#0.0588	Unpaired <i>t</i> test
Sag ratio	0.15 ± 0.03	0.08 ± 0.04	0.1903	Mann–Whitney

m, Month. **p* < 0.05. ***p* < 0.01. ****p* < 0.001. # marginally significant.

excitability, was only observed in MECII stellate cells at the late postsymptomatic time point. In contrast, at the post-symptomatic time point, we found minimal changes in excitability of MECII pyramidal and MECIII excitatory neurons, suggesting that these neurons are unlikely to drive memory impairments in 3xTg mice.

Although we aimed for equivalent male and female mice in all groups, based on available animals our sample sizes ended up skewed across sexes, with unequal numbers of cells from each sex (Table 2). To account for any confounds related to the distribution of sexes, we repeated the analysis of our core findings using only female mice. Overall, our primary findings were consistent when using females only. At 3 months of age, in female 3xTg mice, MECII stellate and pyramidal cells were hyperexcitable as demonstrated by reduced rheobase (unpaired *t* test, stellate cells, *p* = 0.001; pyramidal cells, *p* = 0.022) and an increased number of evoked action potentials (two-way RM ANOVA, main effect of genotype, stellate cells, *p* = 0.002; pyramidal cells, *p* = 0.006). At the synaptic level, in 3-month-old female 3xTg mice, MECII stellate cells had marginally reduced E/I frequency (unpaired *t* test, *p* = 0.055) and reduced E/I amplitude (unpaired *t* test, *p* = 0.019). MECII pyramidal cells also had a reduction in both E/I frequency (Mann–Whitney, *p* = 0.042) and amplitude (unpaired *t* test, *p* = 0.017). All these female-only observations are consistent with the results shown in Figures 3–5, where we used both sexes. At 10 months of age, we again found that results in female mice were consistent with the full sample shown in Figures 6–8. For MECII stellate cells in female mice, we found a strong interaction between current-evoked spiking and group (Current × Group Interaction, *p* = 0.0003), indicating increased spiking in 3xTg mice at higher currents. For currents between 250 and 500 pA, we found that stellate cells from female 3xTg mice fired significantly more action potentials compared with controls (main effect of genotype, *p* = 0.045). Furthermore, the E/I frequency of synaptic currents in stellate cells was increased in female 3xTg mice at 10 months of age (unpaired *t* test, *p* = 0.004), similar to the full sample. Together, these results strongly

suggest that our findings are not driven by the unequal distribution of male and female mice across genotypes.

Discussion

Here, we examined neuronal intrinsic excitability and synaptic activity in three subtypes of MEC excitatory cells during the progression of memory impairments in the 3xTg mouse model of AD pathology (Fig. 9). We found that before the onset of memory impairments, early neuronal and synaptic changes were present in all three cell types, but intrinsic changes were generally balanced by opposing shifts in synaptic inputs. Conversely, after the onset of memory impairments, we found that MECII stellate cells were uniquely hyperexcitable, with both increased intrinsic hyperexcitability and increased synaptic excitation relative to inhibition. Together, these data suggest that there are compensatory mechanisms in place that enhance inhibitory inputs onto MECII stellate cells at the early time point, but these mechanisms become compromised during the progression of memory impairments, exacerbating the increased excitability observed in MECII stellate cells. This increased excitability in stellate cells may contribute to memory impairments as stellate cells are necessary for spatial memory (Tennant et al., 2018), and increased excitability in these cells is sufficient to drive hippocampal remapping and memory impairments in control mice (Kanter et al., 2017). Thus, the increased excitability we observed in MECII stellate cells at the 10-month time point is a potential mechanism that may directly contribute to spatial memory impairment in this 3xTg model of AD pathology.

AD is characterized by two major pathologic hallmarks—the accumulation of extracellular amyloid β ($A\beta$) plaques and intracellular neurofibrillary tangles made of hyperphosphorylated tau. Both of these pathologies seem to affect neuronal excitability and circuit dynamics (Harris et al., 2020). In general, studies have found that soluble $A\beta$ oligomers in early AD are causally linked to neuronal and circuit hyperexcitability (Brorson et al., 1995; Ye et al., 2003; Busche et al., 2008, 2012; Zott et al., 2019). On the contrary, tau pathology has generally exhibited an opposing effect (Menkes-Caspi et al., 2015; Fu et al., 2017; Busche et al., 2019; Marinković et al., 2019). In the 3xTg mouse model of AD pathology, which has both amyloid and tau mutations, intracellular $A\beta$ immunoreactivity is apparent at 3–4 months of age in the neocortex, whereas extracellular plaques appear ~6 months in frontal cortex and become evident in entorhinal cortex and hippocampus by 12 months (Oddo et al., 2003; Billings et al., 2005; Belfiore et al., 2019). Thus, early accumulation of toxic $A\beta$ oligomers (Busche et al., 2012; Mucke and Selkoe, 2012; Xu et al., 2015; Busche and Konnerth, 2016) in 3-month-old 3xTg mice may drive the observed changes in neuronal intrinsic excitability and synaptic transmission at this early stage. Phosphorylated tau has also been detected in the hippocampus and cortex as early as 4 months of age in 3xTg mice and is highly prominent by 12 months of age (Belfiore et al., 2019; Javonillo et al., 2022). We observed that by 10 months of age, neuronal excitability became largely normalized in MECII pyramidal neurons and MECIII excitatory neurons, which could be the result of opposing effects of $A\beta$ and tau pathologies. Here, we may have captured these evolving pathologies represented in the excitability profiles of MEC excitatory neurons.

AD causes complex changes in the number and function of voltage-gated ion channels, such as potassium (Sesti, 2016; Villa et al., 2020) and sodium channels (Brown et al., 2011; Verret et al., 2012). Here, we observed early excitability changes in the MEC of

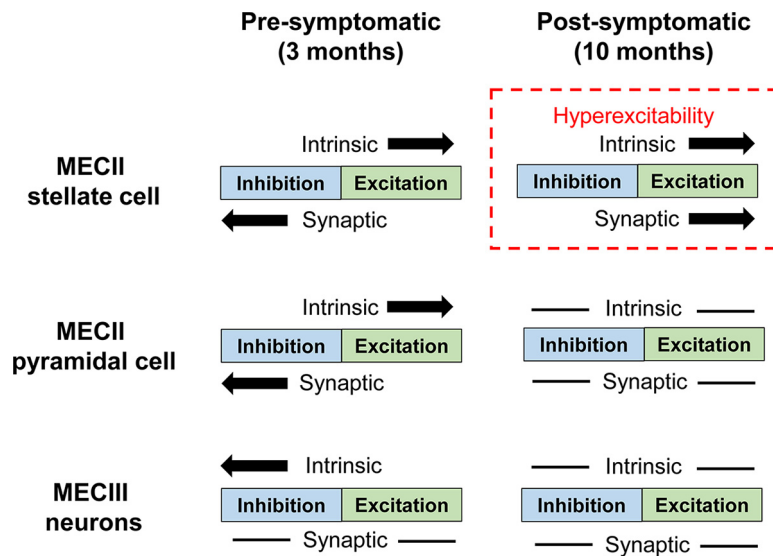


Figure 9. Summary of intrinsic and synaptic changes in excitability across MECII stellate cells, MECII pyramidal cells, and MECIII neurons in 3xTg mice. Progressive changes in intrinsic and synaptic excitability in MECII stellate cells may lead to cell-type-specific hyperexcitability in 3xTg mice. At the early presymptomatic time point (3 months), neuronal intrinsic excitability changes in young 3xTg mice are matched by alterations in synaptic excitation and inhibition in a way that helps to maintain overall excitability in MEC neurons. At the late postsymptomatic time point (10 months), although the intrinsic and synaptic excitability in MECII pyramidal cells and MECIII neurons have largely normalized, MECII stellate cells in 3xTg mice remain hyperexcitable both at the intrinsic and synaptic levels. This loss of homeostatic balance may cause local network hyperexcitability, disrupt downstream hippocampus activity, and lead to deficits in spatial memory.

3xTg mice, even before the onset of memory impairments, which may be caused by distinct changes in voltage-gated ion channels in different cell types at different time points. For example, both MECII stellate and pyramidal cells in 3-month-old 3xTg mice were hyperexcitable, demonstrated by an increased number of evoked action potentials and reduced rheobase (Figs. 3, 4). This hyperexcitability could be caused by an upregulation of voltage-gated sodium channels (Gu and Haddad, 2001; Joca et al., 2012; Randall et al., 2012) and/or downregulation of potassium channels such as Kv1.1 (Xian and Nicol, 2007). However, in pyramidal cells, but not stellate cells, increased input resistance (Table 3) was observed that can also lead to increased spike generation in response to somatic current injections. This increased input resistance may be caused by changes in the expression and/or membrane distribution of hyperpolarization-activated channels, such as Kir2.1 internalization (Pignatelli et al., 2019). Therefore, although early hyperexcitability was present in both cell types, distinct voltage-gated ion channels may play a regulatory role in MECII stellate and pyramidal cells. Future studies using single-nucleus RNA sequencing or patch-sequencing in defined cell types would be particularly informative about the specific channels that are altered to drive hyperexcitability or hypoexcitability in each of the MEC cell populations. One caveat to our intrinsic excitability measurements is that we did not apply any blockers of glutamatergic and/or GABAergic transmission during our recordings. This allowed us to maximize the use of transgenic mice by recording synaptic transmission and intrinsic excitability in the same cells, but it is possible that those synaptic inputs influenced certain intrinsic excitability measures. However, any effects of synaptic input on these intrinsic excitability measures are typically transient and therefore are likely to have a minimal impact on these measures.

Interestingly, each subtype of MECII excitatory neurons recruited distinct synaptic mechanisms in balancing the increased intrinsic excitability at 3 months of age, with stellate cells receiving increased inhibition and pyramidal cells receiving reduced

excitation compared with WT mice. This distinction is particularly interesting considering that this enhanced inhibition onto stellate cells was lost at 10 months when those cells were still hyperexcitable, exacerbating overall network hyperactivity. This change in synaptic currents may be because of interneuron dysfunction, which has been observed in the hippocampus (Palop et al., 2007; Leung et al., 2012; Hazra et al., 2013; Schmid et al., 2016; Prince et al., 2021), parietal cortex (Verret et al., 2012; Chen et al., 2018), and lateral entorhinal cortex (Pettrache et al., 2019) in several mouse models of AD pathology. Therefore, time-dependent changes in the number, function, and synaptic innervation of interneurons may drive the switch in synaptic inhibition from high to low in stellate cells. Moreover, both presynaptic and postsynaptic mechanisms are involved in the regulation of excitation to inhibition ratio. Alterations in the frequency of postsynaptic currents most often reflect changes in presynaptic release probability and presynaptic firing frequency, whereas alterations in the amplitude of spontaneous events can be affected by a mixture of presynaptic and postsynaptic mechanisms, although they are most strongly affected by postsynaptic receptor density (Choi and Lovinger, 1997). We observed overall opposite changes in the E/I ratio of MECII stellate cells in 3xTg mice between 3 months of age (Fig. 3G,K) and 10 months of age (Fig. 6G,K), with potentially distinct presynaptic and postsynaptic mechanisms. At the early time point, MECII stellate cells had reduced E/I frequency and amplitude (Fig. 3G,K), indicating both presynaptic and postsynaptic mechanisms working together to raise overall inhibition in response to early hyperexcitability. At the late time point, increased IPSC amplitude observed at the early time point (Fig. 3I) was lost (Fig. 6I). Moreover, there was a switch from reduction to increase in the E/I frequency (Fig. 6G), suggesting loss of presynaptic E/I balance that further exacerbates the overall network excitability on top of neuronal intrinsic hyperexcitability (Fig. 6C). Thus, presynaptic and postsynaptic mechanisms work together at the early time point to balance neuronal hyperexcitability, whereas at the late time point, loss of increased postsynaptic inhibition together with increased E/I frequency from presynaptic input may synergistically cause overexcitation in

this circuit. Future studies recording miniature postsynaptic currents in the presence of tetrodotoxin would help to further clarify the mechanisms underlying these synaptic changes in different MEC cell types over time.

Sex differences have been widely reported in AD with a larger number of women than men having AD worldwide (Alzheimer's Association, 2023), and women have faster cognitive decline after diagnosis (Ferretti et al., 2018). In the 3xTg model, female mice displayed more prominent amyloid plaques, neuroinflammation, and spatial memory deficits than male 3xTg mice (Hirata-Fukae et al., 2008; Yang et al., 2018), as well as sex-dependent changes in neurophysiological properties in deep layers of MEC (Arsenault et al., 2020). Although we have used both sexes in our study, the number of cells recorded from each sex is not powered to determine sex differences. Although our female-only analyses generated consistent results compared with using both sexes (see above, Results), more experiments with properly powered numbers of male and female mice are necessary to investigate any potential sex differences in the cellular properties of MEC cells in the 3xTg mouse model of AD pathology.

Overall, the progressive and cell-type-specific changes in these three types of excitatory neurons in the MEC indicate complex changes associated with AD pathology. Understanding this progression will enable us to develop early treatments and interventions to slow down or halt the development of cognitive dysfunction in this disease. Further studies using cell-type-specific optogenetic, chemogenetic, or pharmacogenetic manipulations will help elucidate any causal relationship between abnormal neural activity in the MEC and the progression of memory deficits in Alzheimer's disease.

References

- Alonso A, Klink R (1993) Differential electroresponsiveness of stellate and pyramidal-like cells of medial entorhinal cortex layer II. *J Neurophysiol* 70:128–143.
- Alzheimer's Association (2023) Alzheimer's disease facts and figures. *Alzheimer's Dement* 19:1598–1695.
- Arsenault D, Tremblay C, Emond V, Calon F (2020) Sex-dependent alterations in the physiology of entorhinal cortex neurons in old heterozygous 3xTg-AD mice. *Biol Sex Differ* 11:63.
- Belfiore R, Rodin A, Ferreira E, Velazquez R, Branca C, Caccamo A, Oddo S (2019) Temporal and regional progression of Alzheimer's disease-like pathology in 3xTg-AD mice. *Aging Cell* 18:e12873.
- Billings LM, Oddo S, Green KN, McGaugh JL, LaFerla FM (2005) Intra-neuronal Abeta causes the onset of early Alzheimer's disease-related cognitive deficits in transgenic mice. *Neuron* 45:675–688.
- Booth CA, Ridler T, Murray TK, Ward MA, de Groot E, Goodfellow M, Phillips KG, Randall AD, Brown JT (2016a) Electrical and network neuronal properties are preferentially disrupted in dorsal, but not ventral, medial entorhinal cortex in a mouse model of tauopathy. *J Neurosci* 36:312–324.
- Booth CA, Witton J, Nowacki J, Tsaneva-Atanasova K, Jones MW, Randall AD, Brown JT (2016b) Altered intrinsic pyramidal neuron properties and pathway-specific synaptic dysfunction underlie aberrant hippocampal network function in a mouse model of tauopathy. *J Neurosci* 36:350–363.
- Braak H, Braak E (1991) Neuropathological staging of Alzheimer-related changes. *Acta Neuropathol* 82:239–259.
- Bronson JR, Bindokas VP, Iwama T, Marcuccilli CJ, Chisholm JC, Miller RJ (1995) The Ca²⁺ influx induced by β -amyloid peptide 25–35 in cultured hippocampal neurons results from network excitation. *J Neurobiol* 26:325–338.
- Brown JT, Chin J, Leiser SC, Pangalos MN, Randall AD (2011) Altered intrinsic neuronal excitability and reduced Na⁺ currents in a mouse model of Alzheimer's disease. *Neurobiol Aging* 32:2109.e1–e14.
- Buckner RL, Snyder AZ, Shannon BJ, LaRossa G, Sachs R, Fotenos AF, Sheline YI, Klunk WE, Mathis CA, Morris JC, Mintun MA (2005) Molecular, structural, and functional characterization of Alzheimer's disease: evidence for a relationship between default activity, amyloid, and memory. *J Neurosci* 25:7709–7717.
- Busche MA, Konnerth A (2016) Impairments of neural circuit function in Alzheimer's disease. *Philos Trans R Soc Lond B Biol Sci* 371:20150429.
- Busche MA, Eichhoff G, Adelsberger H, Abramowski D, Wiederhold K-H, Haass C, Staufenbiel M, Konnerth A, Garaschuk O (2008) Clusters of hyperactive neurons near amyloid plaques in a mouse model of Alzheimer's disease. *Science* 321:1686–1689.
- Busche MA, Chen X, Henning HA, Reichwald J, Staufenbiel M, Sakmann B, Konnerth A (2012) Critical role of soluble amyloid- β for early hippocampal hyperactivity in a mouse model of Alzheimer's disease. *Proc Natl Acad Sci U S A* 109:8740–8745.
- Busche MA, Wegmann S, Dujardin S, Commins C, Schiantarelli J, Klickstein N, Kamath TV, Carlson GA, Nelken I, Hyman BT (2019) Tau impairs neural circuits, dominating amyloid- β effects, in Alzheimer models *in vivo*. *Nat Neurosci* 22:57–64.
- Cacucci F, Yi M, Wills TJ, Chapman P, O'Keefe J (2008) Place cell firing correlates with memory deficits and amyloid plaque burden in Tg2576 Alzheimer mouse model. *Proc Natl Acad Sci U S A* 105:7863–7868.
- Cai DJ, et al. (2016) A shared neural ensemble links distinct contextual memories encoded close in time. *Nature* 534:115–118.
- Canto CB, Witter MP (2012) Cellular properties of principal neurons in the rat entorhinal cortex. II. The medial entorhinal cortex. *Hippocampus* 22:1277–1299.
- Chen L, Saito T, Saido TC, Mody I (2018) Novel quantitative analyses of spontaneous synaptic events in cortical pyramidal cells reveal subtle parvalbumin-expressing interneuron dysfunction in a knock-in mouse model of Alzheimer's disease. *eNeuro* 5:ENEURO.0059-18.2018.
- Chen L, Cummings KA, Mau W, Zaki Y, Dong Z, Rabinowitz S, Clem RL, Shuman T, Cai DJ (2020) The role of intrinsic excitability in the evolution of memory: significance in memory allocation, consolidation, and updating. *Neurobiol Learn Mem* 173:107266.
- Choi S, Lovinger DM (1997) Decreased frequency but not amplitude of quantal synaptic responses associated with expression of corticostriatal long-term depression. *J Neurosci* 17:8613–8620.
- Creighton SD, Mendell AL, Palmer D, Kalisch BE, MacLusky NJ, Prado VF, Prado MAM, Winters BD (2019) Dissociable cognitive impairments in two strains of transgenic Alzheimer's disease mice revealed by a battery of object-based tests. *Sci Rep* 9:57.
- Daoudal G, Debanne D (2003) Long-term plasticity of intrinsic excitability: learning rules and mechanisms. *Learn Mem* 10:456–465.
- Davis KE, Easton A, Eacott MJ, Gigg J (2013) Episodic-like memory for what-where-which occasion is selectively impaired in the 3xTgAD mouse model of Alzheimer's disease. *J Alzheimers Dis* 33:681–698.
- Davis KE, Fox S, Gigg J (2014) Increased hippocampal excitability in the 3xTgAD mouse model for Alzheimer's disease *in vivo*. *PLoS One* 9:e91203.
- Dickson CT, Mena AR, Alonso A (1997) Electroresponsiveness of medial entorhinal cortex layer III neurons *in vitro*. *Neuroscience* 81:937–950.
- Disterhoft JF, Oh MM (2006) Learning, aging and intrinsic neuronal plasticity. *Trends Neurosci* 29:587–599.
- Fernandez FR, Via G, Canavier CC, White JA (2022) Kinetics and connectivity properties of parvalbumin- and somatostatin-positive inhibition in layer 2/3 medial entorhinal cortex. *eNeuro* 9:ENEURO.0441-21.2022.
- Ferretti MT, Iulita MF, Cavado E, Chiesa PA, Dimech AS, Chadha AS, Baracchi F, Girouard H, Misoch S, Giacobini E, Depypere H, Hampel H (2018) Sex differences in Alzheimer disease—the gateway to precision medicine. *Nat Rev Neurol* 14:457–469.
- Forner S, Baglietto-Vargas D, Martini AC, Trujillo-Estrada L, LaFerla FM (2017) Synaptic impairment in Alzheimer's disease: a dysregulated symphony. *Trends Neurosci* 40:347–357.
- Frazzini V, Guarnieri S, Bombà M, Navarra R, Morabito C, Mariggiò MA, Sensi SL (2016) Altered Kv2.1 functioning promotes increased excitability in hippocampal neurons of an Alzheimer's disease mouse model. *Cell Death Dis* 7:e2100.
- Fu H, Rodriguez GA, Herman M, Emrani S, Nahmani E, Barrett G, Figueroa HY, Goldberg E, Hussaini SA, Duff KE (2017) Tau pathology induces excitatory neuron loss, grid cell dysfunction, and spatial memory deficits reminiscent of early Alzheimer's disease. *Neuron* 93:533–541.e5.

- Fuchs EC, Neitz A, Pinna R, Melzer S, Caputi A, Monyer H (2016) Local and distant input controlling excitation in layer II of the medial entorhinal cortex. *Neuron* 89:194–208.
- Gloveli T, Schmitz D, Empson RM, Dugladze T, Heinemann U (1997) Morphological and electrophysiological characterization of layer III cells of the medial entorhinal cortex of the rat. *Neuroscience* 77:629–648.
- Gómez-Isla T, Price JL, McKeel DW, Morris JC, Growdon JH, Hyman BT (1996) Profound loss of layer II entorhinal cortex neurons occurs in very mild Alzheimer's disease. *J Neurosci* 16:4491–4500.
- Gstir R, Schaffner S, Scheideler M, Misslinger M, Griehl M, Daschil N, Humpel C, Obermair GJ, Schmucker C, Striessnig J, Flucher BE, Hüttenhofer A (2014) Generation of a neuro-specific microarray reveals novel differentially expressed noncoding RNAs in mouse models for neurodegenerative diseases. *RNA* 20:1929–1943.
- Gu XQ, Haddad GG (2001) Decreased neuronal excitability in hippocampal neurons of mice exposed to cyclic hypoxia. *J Appl Physiol* (1985) 91:1245–1250.
- Harris SS, Wolf F, De Strooper B, Busche MA (2020) Tipping the scales: peptide-dependent dysregulation of neural circuit dynamics in Alzheimer's disease. *J Neurosci* 107:417–435.
- Hazra A, Gu F, Aulakh A, Berridge C, Eriksen JL, Ziburkus J (2013) Inhibitory neuron and hippocampal circuit dysfunction in an aged mouse model of Alzheimer's disease. *PLoS One* 8:e64318.
- Heggland I, Kvello P, Witter MP (2019) Electrophysiological characterization of networks and single cells in the hippocampal region of a transgenic rat model of Alzheimer's disease. *eNeuro* 6:ENEURO.0448-17.2019.
- Hirata-Fukae C, et al. (2008) Females exhibit more extensive amyloid, but not tau, pathology in an Alzheimer transgenic model. *Brain Res* 1216:92–103.
- Hyman BT, Van Hoesen GW, Kromer LJ, Damasio AR (1986) Perforant pathway changes and the memory impairment of Alzheimer's disease. *Ann Neurol* 20:472–481.
- Igarashi KM (2023) Entorhinal cortex dysfunction in Alzheimer's disease. *Trends Neurosci* 46:124–136.
- Javonillo DI, et al. (2022) Systematic phenotyping and characterization of the 3xTg-AD mouse model of Alzheimer's disease. *Front Neurosci* 15:785276.
- Joca HC, Cruz-Mendes Y, Oliveira-Abreu K, Maia-Joca RPM, Barbosa R, Lemos TL, Lacerda Beirão PS, Leal-Cardoso JH (2012) Carvacrol decreases neuronal excitability by inhibition of voltage-gated sodium channels. *J Nat Prod* 75:1511–1517.
- Jun H, Bramian A, Soma S, Saito T, Saido TC, Igarashi KM (2020) Disrupted place cell remapping and impaired grid cells in a knockin model of Alzheimer's disease. *Neuron* 107:1095–1112.e6.
- Kaczorowski CC, Sametsky E, Shah S, Vassar R, Disterhoft JF (2011) Mechanisms underlying basal and learning-related intrinsic excitability in a mouse model of Alzheimer's disease. *Neurobiol Aging* 32:1452–1465.
- Kanter BR, Lykken CM, Avesar D, Weible A, Dickinson J, Dunn B, Borgesius NZ, Roudi Y, Kentros CG (2017) A novel mechanism for the grid-to-place cell transformation revealed by transgenic depolarization of medial entorhinal cortex layer II. *Neuron* 93:1480–1492.e6.
- Kerrigan TL, Brown JT, Randall AD (2014) Characterization of altered intrinsic excitability in hippocampal CA₁ pyramidal cells of the A β -overproducing PDAPP mouse. *Neuropharmacology* 79:515–524.
- Kitamura T, Pignatelli M, Suh J, Kohara K, Yoshiki A, Abe K, Tonegawa S (2014) Island cells control temporal association memory. *Science* 343:896–901.
- Klink R, Alonso A (1997) Morphological characteristics of layer II projection neurons in the rat medial entorhinal cortex. *Hippocampus* 7:571–583.
- Leung L, Andrews-Zwilling Y, Yoon SY, Jain S, Ring K, Dai J, Wang MM, Tong L, Walker D, Huang Y (2012) Apolipoprotein E4 causes age- and sex-dependent impairments of hilar GABAergic interneurons and learning and memory deficits in mice. *PLoS One* 7:e35569.
- Mably AJ, Gereke BJ, Jones DT, Colgin LL (2017) Impairments in spatial representations and rhythmic coordination of place cells in the 3xTg mouse model of Alzheimer's disease. *Hippocampus* 27:378–392.
- Marcantoni A, Raymond EF, Carbone E, Marie H (2014) Firing properties of entorhinal cortex neurons and early alterations in an Alzheimer's disease transgenic model. *Pflugers Arch Eur Arch* 466:1437–1450.
- Marinković P, Blumenstock S, Goltstein PM, Korzhova V, Peters F, Knebl A, Herms J (2019) *In vivo* imaging reveals reduced activity of neuronal circuits in a mouse tauopathy model. *Brain* 142:1051–1062.
- Masdeu JC, Zubieta JL, Arbuzo J (2005) Neuroimaging as a marker of the onset and progression of Alzheimer's disease. *J Neurosci* 23:55–64.
- Menkes-Caspi N, Yamin HG, Kellner V, Spires-Jones TL, Cohen D, Stern EA (2015) Pathological tau disrupts ongoing network activity. *Neuron* 85:959–966.
- Mucke L, Selkoe DJ (2012) Neurotoxicity of amyloid β -protein: synaptic and network dysfunction. *Cold Spring Harb Perspect Med* 2:a006338.
- Murai T, Okuda S, Tanaka T, Ohta H (2007) Characteristics of object location memory in mice: behavioral and pharmacological studies. *Physiol Behav* 90:116–124.
- Oddo S, Caccamo A, Shepherd JD, Murphy MP, Golde TE, Kaye R, Metherate R, Mattson MP, Akbari Y, LaFerla FM (2003) Triple-transgenic model of Alzheimer's disease with plaques and tangles: intracellular A β and synaptic dysfunction. *Neuron* 39:409–421.
- Oh MM, Oliveira FA, Disterhoft JF (2010) Learning and aging related changes in intrinsic neuronal excitability. *Front Aging Neurosci* 2:2.
- Ohara S, Gianatti M, Ito K, Berndtsson CH, Doan TP, Kitanishi T, Mizuseki K, Iijima T, Tsutsui KI, Witter MP (2019) Entorhinal layer II calbindin-expressing neurons originate widespread telencephalic and intrinsic projections. *Front Syst Neurosci* 13:54.
- Ohno M, Sametsky EA, Younkin LH, Oakley H, Younkin SG, Citron M, Vassar R, Disterhoft JF (2004) BACE1 deficiency rescues memory deficits and cholinergic dysfunction in a mouse model of Alzheimer's disease. *Neuron* 41:27–33.
- Palop JJ, Mucke L (2010) Amyloid-beta-induced neuronal dysfunction in Alzheimer's disease: from synapses toward neural networks. *Nat Neurosci* 13:812–818.
- Palop JJ, Chin J, Roberson ED, Wang J, Thwin MT, Bien-Ly N, Yoo J, Ho KO, Yu G-Q, Kreitzer A, Finkbeiner S, Noebels JL, Mucke L (2007) Aberrant excitatory neuronal activity and compensatory remodeling of inhibitory hippocampal circuits in mouse models of Alzheimer's disease. *Neuron* 55:697–711.
- Petrache AL, Rajulawalla A, Shi A, Wetzel A, Saito T, Saido TC, Harvey K, Ali AB (2019) Aberrant excitatory-inhibitory synaptic mechanisms in entorhinal cortex microcircuits during the pathogenesis of Alzheimer's disease. *Cereb Cortex* 29:1834–1850.
- Pignatelli M, Ryan TJ, Roy DS, Lovett C, Smith LM, Muralidhar S, Tonegawa S (2019) Engram cell excitability state determines the efficacy of memory retrieval. *Neuron* 101:274–284.e5.
- Philipsberg PA, Christenson Wick Z, Diego KS, Vaughan N, Galas A, Jurkowski A, Feng Y, Vetere LM, Chen L, Soler I, Cai DJ, Shuman T (2023) Chronotate: An open-source tool for manual timestamping and quantification of animal behavior. *Neurosci Lett* 814:137461.
- Prince SM, Paulson AL, Jeong N, Zhang L, Amigues S, Singer AC (2021) Alzheimer's pathology causes impaired inhibitory connections and reactivation of spatial codes during spatial navigation. *Cell Rep* 35:109008.
- Randall AD, Booth C, Brown JT (2012) Age-related changes to Na⁺ channel gating contribute to modified intrinsic neuronal excitability. *Neurobiol Aging* 33:2715–2720.
- Ray S, Naumann R, Burgalossi A, Tang Q, Schmidt H, Brecht M (2014) Grid-layout and theta-modulation of layer 2 pyramidal neurons in medial entorhinal cortex. *Science* 343:891–896.
- Saito T, Matsuba Y, Mihira N, Takano J, Nilsson P, Itohara S, Iwata N, Saido TC (2014) Single App knock-in mouse models of Alzheimer's disease. *Nat Neurosci* 17:661–663.
- Schmid LC, Mittag M, Poll S, Steffen J, Wagner J, Geis HR, Schwarz I, Schmidt B, Schwarz MK, Remy S, Fuhrmann M (2016) Dysfunction of somatostatin-positive interneurons associated with memory deficits in an Alzheimer's disease model. *Neuron* 92:114–125.
- Sehgal M, Song C, Ehlers VL, Moyer JR (2013) Learning to learn—intrinsic plasticity as a metaplasticity mechanism for memory formation. *Neurobiol Learn Mem* 105:186–199.
- Sesti F (2016) Oxidation of K⁺ channels in aging and neurodegeneration. *Aging Dis* 7:130–135.
- Shuman T, et al. (2020) Breakdown of spatial coding and interneuron synchronization in epileptic mice. *Nat Neurosci* 23:229–238.
- Stevens LM, Brown RE (2015) Reference and working memory deficits in the 3xTg-AD mouse between 2 and 15-months of age: a cross-sectional study. *Behav Brain Res* 278:496–505.
- Stranahan AM, Mattson MP (2010) Selective vulnerability of neurons in layer II of the entorhinal cortex during aging and Alzheimer's disease. *Neural Plast* 2010:108190.

- Suh J, Rivest AJ, Nakashiba T, Tominaga T, Tonegawa S (2011) Entorhinal cortex layer III input to the hippocampus is crucial for temporal association memory. *Science* 334:1415–1420.
- Tennant SA, Fischer L, Garden DLF, Gerlei KZ, Martinez-Gonzalez C, McClure C, Wood ER, Nolan MF (2018) Stellate cells in the medial entorhinal cortex are required for spatial learning. *Cell Rep* 22:1313–1324.
- Varga C, Lee SY, Soltesz I (2010) Target-selective GABAergic control of entorhinal cortex output. *Nat Neurosci* 13:822–824.
- Verret L, Mann EO, Hang GB, Barth AMI, Cobos I, Ho K, Devidze N, Masliah E, Kreitzer AC, Mody I, Mucke L, Palop JJ (2012) Inhibitory interneuron deficit links altered network activity and cognitive dysfunction in Alzheimer model. *Cell* 149:708–721.
- Villa C, Suphesiz H, Combi R, Akyuz E (2020) Potassium channels in the neuronal homeostasis and neurodegenerative pathways underlying Alzheimer's disease: an update. *Mech Ageing Dev* 185:111197.
- Wimmer ME, Hernandez PJ, Blackwell J, Abel T (2012) Aging impairs hippocampus-dependent long-term memory for object location in mice. *Neurobiol Aging* 33:2220–2224.
- Witter MP, Canto CB, Couey JJ, Koganezawa N, O'Reilly KC (2014) Architecture of spatial circuits in the hippocampal region. *Philos Trans R Soc B Biol Sci* 369:20120515.
- Xian XC, Nicol GD (2007) Manipulation of the potassium channel Kv1.1 and its effect on neuronal excitability in rat sensory neurons. *J Neurophysiol* 98:2683–2692.
- Xu W, Fitzgerald S, Nixon RA, Levy E, Wilson DA (2015) Early hyperactivity in lateral entorhinal cortex is associated with elevated levels of A β PP metabolites in the Tg2576 mouse model of Alzheimer's disease. *Exp Neurol* 264:82–91.
- Yang JT, Wang ZJ, Cai HY, Yuan L, Hu MM, Wu MN, Qi JS (2018) Sex differences in neuropathology and cognitive behavior in APP/PS1/tau triple-transgenic mouse model of Alzheimer's disease. *Neurosci Bull* 34:736–746.
- Ye CP, Selkoe DJ, Hartley DM (2003) Protofibrils of amyloid β -protein inhibit specific K⁺ currents in neocortical cultures. *Neurobiol Dis* 13:177–190.
- Ying J, Keinath AT, Lavoie R, Vigneault E, El Mestikawy S, Brandon MP (2022) Disruption of the grid cell network in a mouse model of early Alzheimer's disease. *Nat Commun* 13:886.
- Zhang W, Linden DJ (2003) The other side of the engram: experience-driven changes in neuronal intrinsic excitability. *Nat Rev Neurosci* 4:885–900.
- Zott B, Simon MM, Hong W, Unger F, Chen-Engerer HJ, Frosch MP, Sakmann B, Walsh DM, Konnerth A (2019) A vicious cycle of β amyloid-dependent neuronal hyperactivation. *Science* 365:559–565.